International Journal of Nanomedicine

Dovepress
open access to scientific and medical research

Open Access Full Text Article

ORIGINAL RESEARCH

Combinational phototherapy and hypoxia-activated chemotherapy favoring antitumor immune responses

This article was published in the following Dove Press journal:
International Journal of Nanomedicine

Beibei Ma[1,*]
Jie Sheng[1,2,*]
Ping Wang[1]
Zhongying Jiang[1,2]
Entomack Borrathybay[3]

[1]College of Electronic and Information Engineering, Yili Normal University, Micro-nano Electric Sensing Technology and Bionic Devices Key Laboratory, Yining 835000, People's Republic of China; [2]Physics School of Nanjing University, Laboratory of Solid State Microstructures, Nanjing 210093, People's Republic of China; [3]College of Biology and Geography Sciences, Yili Normal University, Yining, Xinjiang, 835000, People's Republic of China

*These authors contributed equally to this work

Background: Tumor metastasis is responsible for most cancer death worldwide, which lacks curative treatment.

Purpose: The objective of this study was to eliminate tumor and control the development of tumor metastasis.

Methods: Herein, we demonstrated a smart nano-enabled platform, in which 2-[2-[2-chloro-3-[(1,3-dihydro-3,3-dimethyl-1-propyl-2h-indol-2-ylidene)ethylidene]-1-cyclohexen-1-yl] ethenyl]-3,3-dimethyl-1-propylindolium iodide (IR780) and tirapazamine (TPZ) were co-loaded in poly(ε-caprolactone)-poly(ethylene glycol) (PEG-PCL) to form versatile nanoparticles (PEG-PCL-IR780-TPZ NPs).

Results: The intelligence of the system was reflected in the triggered and controlled engineering. Specially, PEG-PCL not only prolonged the circulation time of IR780 and TPZ but also promoted tumor accumulation of nanodrugs through enhanced permeability and retention (EPR) effect. Moreover, reactive oxygen species (ROS) generated by IR780 armed by an 808 nm laser irradiation evoked a cargo release. Meanwhile, IR780, as a mitochondria-targeting phototherapy agent exacerbated tumor hypoxic microenvironment and activated TPZ for accomplishing hypoxia-activated chemotherapy. Most significantly, IR780 was capable of triggering immunogenic cell death (ICD) during the synergic treatment. ICD biomarkers as a "danger signal" accelerated dendritic cells (DCs) maturation, and subsequently activated toxic T lymphocytes.

Conclusion: Eventually, antitumor immune responses stimulated by combinational phototherapy and hypoxia-activated chemotherapy revolutionized the current landscape of cancer treatment, strikingly inhibiting tumor metastasis and providing a promising prospect in the clinical application.

Keywords: phototherapy, hypoxia-activated chemotherapy, IR780, tirapazamine, antitumor immune responsive, metastasis

Correspondence: Zhongying Jiang
College of Electronic and Information Engineering, Yili Normal University, Micro-nano Electric Sensing Technology and Bionic Devices Key Laboratory, Yining 835000, People's Republic of China
Tel +86 999 813 7647
Fax +86 25 813 2481
Email jiangzhying@163.com

Entomack Borrathybay
College of Biology and Geography Sciences, Yili Normal University, Yining 835000, Xinjiang People's Republic of China
Tel +86 999 899 6985
Email 1632984092@qq.com

Introduction

Superior strides in antitumor strategies have modestly improved the clinical outcomes, the mortality of tumor still remains high owing to tumor recurrence and metastasis.[1–8] Immunotherapy has been well concerned due to its function of controlling the development of distant metastatic tumor.[9–11] In particular, checkpoint inhibitors and chimeric antigen receptor T-cell immunotherapy have been regarded as crucial tools for cancer treatment.[12–20] Nevertheless, the application of these two strategies is restricted due to serious side effects, high cost, and large individual variations.[21–24] More seriously, some tumor tissues, especially triple-negative breast cancer (TNBC), have

relatively low immune response after treatment of checkpoint inhibitors, which is mainly attributed to "cold" immune microenvironment.[4] Hence, exploring novel and powerful methods to achieve the "hot" immune microenvironment and trigger immune response as a prelude for immunotherapy is particularly crucial.

Immunogenic cell death (ICD) has been reported to a stimulant circumstance to change "cold" immune microenvironment to "hot" immune microenvironment.[25–27] Phototherapy as a minimally invasive treatment strategy has been phenomenally applied to tumor ablation.[28–35] A recent report described that phototherapy induces ICD under laser irradiation.[36] In addition to phototherapy, some other ICD inducers including chemotherapy and ionizing radiation have also been evidenced.[23,37,38] However, several intolerable limitations, such as low drug delivery, ignorable cargo release, and single treatment regimen greatly restrict ICD outcome. It is highly expected that the intelligent engineering of a tumor-responsive drug nano-vehicle, the rational combination of phototherapy and chemotherapy is capable of synergistically offering active breakthroughs against limited ICD efficacy. However, there is little work to achieve the desirable high efficiency.

In this study, we custom-designed PEG-PCL-IR780-TPZ NPs (Figure 1) as a robust nano-carrier system for high-effectively delivering a phototherapy agent (IR780) and a chemotherapy prodrug (TPZ). The $^1O_2$ (one of ROS) generated by IR780 upon an 808-nm laser irradiation released IR780 and TPZ from PEG-PCL-IR780-TPZ NPs after the damage of phospholipid bilayers and achieved a concurrent release.[39–41] IR780 as a mitochondria-targeting phototherapy agent was able to improve the therapeutic efficacy owing to the phototherapy-sensitivity of mitochondria.[42,43] Yang et al reported that TPZ, as a hypoxia-activatable prodrug, had little effect on normal cells but displayed a selectively high toxicity to hypoxic cells.[44–46] They have also proved that IR780

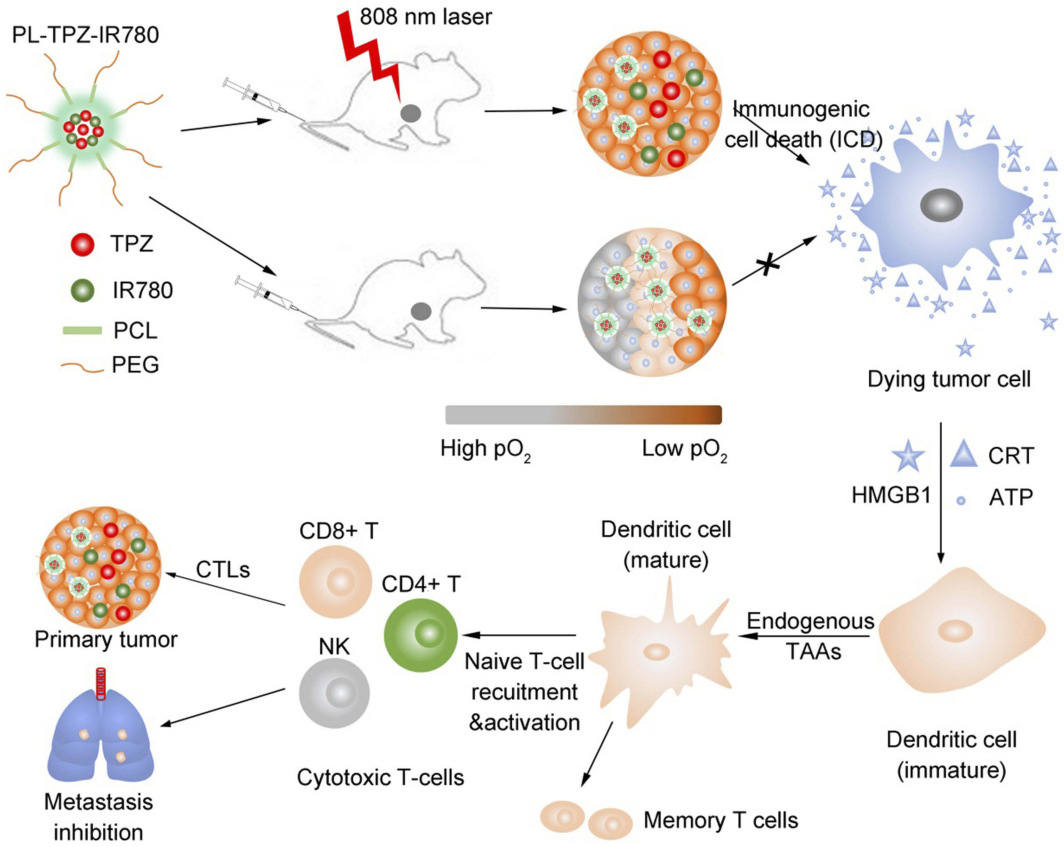

Figure 1 Schematic illustration showing immunotherapy for tumor ablation and metastasis inhibition. After the laser irradiation, immunogenic cell death (ICD) was induced from polyethylene glycol- polycaprolactone-2-[2-[2-Chloro-3-[(1,3-dihydro-3,3-dimethyl-1-propyl-2H-indol-2-ylidene)ethylidene]-1-cycloxen-1-yl]-ethenyl]-3,3-dimethy-1-propyl-1H-indolium iodide-tirapazamine nanoparticles (PEG-PCL-IR780-TPZ NPs)-based synergic phototherapy and hypoxia-activated chemotherapy. Damage-associated molecular patterns (DAMPs) including adenosine triphosphate (ATP), high-motility group box 1 (HMGB1), and calreticulin (CRT) were produced as endogenous potentiators and subsequently promoted dendritic cells (DCs) maturation. Eventually, the naïve T-cells were recruited by mature DCs and cytotoxic T lymphocytes (CTLs) including CD8+T, CD4+T, and natural killer (NK) cells were elicited, which played an indispensable in ablating primary tumor and controlling tumor metastasis.

exacerbated tumor hypoxic microenvironment during photodynamic therapy process, which would stimulate TPZ to generate toxic oxidizing radical species (hydroxyl radical and benzotriazinyl radical) through a single-electron reduction reaction.[47] With optimal laser irradiation time, combinational phototherapy and hypoxia-activated chemotherapy elicit ICD-mediated adaptive immune response through the tremendous generation of endogenous potentiators, including high-motility group box 1 (HMGB1), adenosine triphosphate (ATP) and calreticulin (CRT).[48–50] Furtherly, the endogenous potentiators are recognized by dendritic cells (DCs) and contribute to DC maturation.[51] Consequently, the naive T-cells are recruited by mature DCs to activate cytotoxic T lymphocytes (CTLs), including cluster differentiation (CD)8+T, CD4+T, and NK cells, thereafter ablating primary tumor and controlling tumor metastasis.[48,52,53] In a word, our study provided three significant findings. First, we disclosed a nano-enabled triggered and controlled nanovehicle. Second, we highlighted that phototherapy of PEG-PCL-IR780-TPZ NPs could exacerbate tumor hypoxia and invoke a hypoxia-activated chemotherapy. Third, we revealed antitumor immune responses stimulated by combinational phototherapy and hypoxia-activated chemotherapy dramatically inhibited tumor metastasis.

Materials and methods

Materials

Tirapazamine (TPZ), ε-caprolactone, 2-[2-[2-chloro-3-[(1,3-dihydro-3,3-dimethyl-1-propyl-2h-indol-2-ylidene) ethylidene]-1-cyclohexen-1-yl]ethenyl]-3,3-dimethyl-1-propylindolium iodide (IR780 iodide), 2,2,6,6-tetramethylpiperidine-(TEMP) diethylene glycol, and N,N′-dimethylformamide were purchased from Sigma-Aldrich (Shanghai, China). (3-(4,5)-dimethylthiahiazo (-z-y1)-3,5-di- phenytetrazoliumromide) MTT assay, 4',6-diamidino-2-phenylindole (DAPI), Calcein-AM/propidium iodide (PI) double staining assay, Dulbecco's modified eagle medium (DMEM), serum-free RPMI-1640 medium, and fetal bovine serum (FBS) were obtained from KeyGen Bio-tech Co., Ltd. (Nanjing, China). Interleukin 12 (IL-12) ELISA kit, fluorescein isothiocyanate (FITC)-conjugated anti-mouse CD11c antibody, anti-calreticulin (CRT) antibody, FITC-conjugated anti-mouse CD4 antibody, P-phycoerythrin (PE)-conjugated anti-mouse CD83 antibody, allophycocyanin (APC)-conjugated anti-mouse CD8 antibody, Peridinin-Chlorophyll-Protein Complex (PerCP)-conjugated anti-mouse CD86 antibody, PE-conjugated anti-mouse CD69 antibody, and Luminescent ATP Detection assay were all brought from Abcam (Shanghai, China). HMGB1 ELISA kit, anti-mouse CD31 antibody, and anti-mouse CD8 antibody were purchased from Bioss (Beijing, China). The secondary anti-rabbit antibody-Alexa Fluor 488 and other fluorescent antibodies were from Beyotime Institute of Biotechnology (Nanjing, China). All chemical reagents were not further purified again. The mouse-derived breast cancer cell line 4T1 cells were cultured in growth media, which was obtained from the Cell Bank of Shanghai Institutes for Biological Science (Shanghai, China). All specific pathogen free (SPF) mice were purchased from the Comparative Medicine Center of Yangzhou University (Yangzhou, China) and housed under pathogen-free environment. The deionized water was used in the experiment, which was purified from Milli-Q (Millipore, 18.2 MΩ cm^{-1}).

Preparation of PEG-PCL-IR780-TPZ nanoparticles

The synthesis procedure of poly(ε-caprolactone)-poly (ethylene glycol) (PEG-PCL) was performed as previously described.[54] PEG-PCL-IR780-TPZ nanoparticles (NPs) were prepared using oil-in-water emulsion solvent diffusion method.[54,55] Briefly, IR780 (2.5 mg) and TPZ (2.5 mg) were dissolved in 10 mL of dichloromethane and PEG-PCL was dissolved in 10 mL of deionized water. They were mixed and self-assembly under ultrasonication. After ultrasonication for 1 hr, the PEG-PCL-IR 780-TPZ NPs were successfully synthesized and pelleted via centrifugation. Subsequently, the samples were washed thrice with deionized water and stored at 4°C.

Characterization of PEG-PCL-IR780-TPZ NPs

The morphology and size of PEG-PCL NPs and PEG-PCL -IR780-TPZ NPs were directly captured using transmission electron microscope (TEM, JEOL-200CX, Tokyo, Japan). The hydrodynamic diameter of each type of particles was measured by Zetasizer Nano-ZS90 (DLS, UK). UV-vis absorption spectra were determined using the UV-3600 spectrophotometer (Shimadzu, Tokyo, Japan) to ensure the successful encapsulation of hydrophilic small molecular in PEG-PCL NPs. The drug loading and encapsulation efficiency for both IR780 and TPZ were respectively calculated through the standard curves of IR780 and TPZ determined by UV-vis spectrophotometer. The calculation equations of drug loading and encapsulation are as follows:

$$\text{Drug loading content} = \frac{\text{Weight of the drug in NPs}}{\text{Weight of the NPs}} \times 100\%$$

$$\text{Encapsulation efficiency} = \frac{\text{Weight of the drug in NPs}}{\text{Weight of the feeding drug}} \times 100\%$$

Additionally, PEG-PCL-IR780-TPZ NPs were dissolved in fetal bovine serum (FBS) or phosphate buffered solution (PBS) at 37°C for 8 days to investigate the stability. Subsequently, the hydrodynamic diameter was monitored using DLS instrument. An 808-nm diode laser (LEO photonics Co. Ltd) was used to study the phototherapy. The laser device had a 200 μm diameter fiber, and the beam diameter could be expanded to 11.4 mm with the help of an optical lens, so that to expose the entire tumor area. TEMP spin-trapping electron paramagnetic resonance (EPR) technology was employed to conduct the singlet oxygen detection. The decomposition rate of Na_2-ADPA by PEG-PCL-IR780-TPZ NPs and ICG was recorded at various irradiation times and quantified by the absorbance intensity change of Na_2-ADPA at 378 nm. $^1O_2$ quantum yield was calculated referring to some reports.[56–58]

In vitro infrared (IR) imaging

The in vitro photothermal properties of PEG-PCL-IR780-TPZ NPs were assessed using a thermal imaging camera (Fotric 226, Shanghai, China) under the irradiation of an 808 nm laser with a diminishing density (1.5 W/cm^2, 1.0 W/cm^2, 0.5 W/cm^2, 0.25 W/cm^2). After that, the PEG-PCL -IR780-TPZ NPs solution with different IR780 concentrations (0, 50 μg/mL and 200 μg/mL) in a 6-well plate was further irradiated under the laser power density at 1.0 W/cm^2 for 10 min.

In vitro ROS/hypoxia detection

The ROS/hypoxia effect was evaluated using a ROS-ID® Hypoxia/Oxidative Stress Detection Kit (ENZO, Nanjing, China). First, 4T1 cells were harvested and seeded in a 6-well plate containing DMEM supplemented with 10% FBS for 12 hrs. IR780 (200 μg/mL, according to IR780), PEG-PCL-IR780 (200 μg/mL, according to IR780) and PEG-PCL-IR780-TPZ (200 μg/mL, according to IR780) were added after incubation. Subsequently, cells were exposed to the irradiation of an 808 nm laser (1 W/cm^2) for 5 mins. The hypoxia detection solution was then added into the 6-well plate for another 20 mins in dark. Finally, cells were washed for three times with PBS, and an IX73 fluorescence microscope (Olympus, Japan) was used to capture the images.

MTT assay

In vitro cell cytotoxicity of PEG-PCL-IR780-TPZ NPs was evaluated using the MTT assay. First, 4T1 cells were cultured in a 96-well plate with 2×10^3 cells per well and incubated in DMEM containing 10% FBS under 37°C with 5% CO_2. After incubation for 12 hrs, cells were incubated with different concentrations of PEG-PCL-IR 780 NPs, PEG-PCL-TPZ NPs, and PEG-PCL-IR780-TPZ NPs for 12 hrs. These groups were either irradiated with the laser (1.0 W/cm^2) for 5 mins or not. After that, MTT solution (5 μL) was added into the 96-well plate. After another 4 hrs, the supernatant was discarded and 150 μL of dimethyl sulfoxide (DMSO) was added to dissolve the crystal. Finally, optical density (OD) was measured by a microplate reader (Tecan, Infinite® 200 Pro NanoQuant, Switzerland).

Calcein-AM/PI double staining assay

The calcein-AM/PI double staining was employed to evaluate the cell viability. Briefly, 4T1 cells were seeded into a 6-well plate for 12 hrs under 37°C with 5% CO_2. Cells were incubated with different concentrations of PEG-PCL-IR780 NPs and PEG-PCL-IR780-TPZ NPs for 12 hrs and exposed to an 808 nm laser irradiation (1.0 W/cm^2) for 5 mins or not. The calcein-AM/PI co-staining was performed, and the fluorescence images of live cells, and dead cells were captured using a confocal laser scanning microscope (CLSM, Olympus, FV1000, Tokyo, Japan). The data were analyzed by ImageJ.

Analysis of in vitro ICD biomarkers

To evaluate the in vitro level of immunogenic cell death (ICD) biomarkers, 4T1 cells were co-cultured with IR780 (200 μg/mL, according to IR780), PEG-PCL-IR780 NPs (200 μg/mL, according to IR780) and PEG-PCL-IR780-TPZ NPs (200 μg/mL, according to IR780). After incubation for 12 hrs, an 808 nm laser irradiation was performed for 5 min (the power density of the laser is 1 W/cm^2) or not. After another 3 hrs, the supernatant was collected for detecting the release of HMGB1 and/or ATP by ELISA and a chemiluminescence determination kit (Luminescent ATP Detection Assay (Abcam)). Next, 4T1 cells were washed twice with PBS and fixed with paraformaldehyde (4%) for 15 mins. After PBS washing, Bull Serum

Albumin (BSA, 6% w/v, incubation: 60 min) was used to block non-specific binding for the antibody. 4T1 cells were then incubated with the primary antibody (anti-CRT antibody, dilution 1:100) overnight at 4°C. Afterward, cells were washed three times with PBS and incubated with Alexa Fluor 488-conjugated secondary antibody (dilution 1:100) in dark at room temperature for 60 mins. Finally, cells were washed and stained with DAPI solution. The fluorescence images were captured using CLSM.

Evaluation of DC maturation

To investigate the DCs maturation, bone marrow-derived DCs (BMDCs) were harvested from mice bone marrow according to the reported method.[59] First, the healthy BALB/c mouse (5 weeks old) was sacrificed, and bone marrow cells were collected under specific pathogen-free condition. Red blood cell lysis solution was added to purify BMDCs. After that, cells were cultured in serum-free RPMI-1640 medium supplemented with 10% interleukin-4 (IL-4, 10 ng/mL) and granulocyte-macrophage colony-stimulating factor (GM-CSF, 10 ng/mL) at 37°C with 5% CO_2. After incubation for seven days, the purified BMDCs were obtained. Meanwhile, cells were incubated with IR780 (200 μg/mL, according to IR780), PEG-PCL-IR780 NPs (200 μg/mL, according to IR780) and PEG-PCL-IR780-TPZ NPs (200 μg/mL, according to IR780). An 808 nm laser irradiation (1 W/cm^2, 5 mins) for 24 hrs was employed to trigger the DC maturation. Cells were stained with FITC-conjugated anti-mouse CD11c antibody, PE-conjugated anti-mouse CD83 antibody, PerCP-conjugated anti-mouse CD86 antibody, and then assessed using flow cytometry. Meanwhile, the level of IL-12 effector in the supernatant was estimated using IL-12 ELISA kits as a protocol of reagent.

The xenograft mice tumor models

The healthy female BALB/c mice (5 weeks old) were purchased from Comparative Medicine Centre of Yangzhou University housed under specific pathogen-free environment. Animal experiments were approved by the Care Committee of Nanjing University (including guidelines for animal care & use, and guidelines for euthanasia of mice, Protocol #: 20180212-013). A total of 5×10^6 4T1 cells per mice were subcutaneously injected. Tumor volume was monitored every three days using a vernier caliper. Three days after mice inoculated with 4T1 cells on the right armpit, the second batch of 4T1 cells (5×10^6) was intravenously injected through tail to establish the artificial mimic metastatic model.

In vivo IR imaging

The photothermal effect was evaluated using infrared (IR) thermal camera to ensure the in vivo effective therapy. Briefly, 4T1-tumor-bearing mice were intravenously injected with PBS or PEG-PCL-IR780-TPZ NPs (1.5 mg/kg, according to IR780). Twelve hours later, 4T1-tumor-bearing mice were irradiated by an 808 nm laser for 10 mins at the power density of 1 W/cm^2. All thermographs were analyzed using the Fotric AnalyzIR software.

In vivo antitumor efficacy

For assessing the therapy efficacy of PEG-PCL-IR780-TPZ NPs, 4T1-tumor-bearing mice were randomly divided into four groups, including PBS, IR780 (1.5 mg/kg, according to IR780), PEG-PCL-IR780 (1.5 mg/kg, according to IR780) and PEG-PCL-IR780-TPZ (1.5 mg/kg, according to IR780). Mice in the PBS group were administrated with 100 μL of PBS as negative controls. Mice in the other groups were treated with 100 μL of nanoparticles via intravenous injection, followed by an 808 nm laser irradiation (1 W/cm^2) for 5 mins. The average tumor volume was recorded. Relative tumor volume (RTV) was calculated as follows: $RTV=V/V_0$, in which V was indicative of the volume recorded every three days and V_0 was indicative of primitive volume. After the final treatment, the mice were humanely sacrificed for harvesting major organs that were subjected to further histopathology analysis.

Histopathology analysis

Organs and tumor tissues were harvested, washed three times with PBS, and immediately fixed in paraformaldehyde solution (4% w/v) for one day. Afterward, the tissues were embedded and sectioned to 30 μm slices. Finally, the slices were stained using immunohistochemistry (IHC) staining (Ki67 and HIF), immunofluorescence staining (CD31), and hematoxylin and eosin (H&E).

In vivo micro-positron emission tomography (PET) imaging

The evaluation of tumor hypoxia was carried out using micro-PET imaging. Mice in each treatment group (PBS, IR780+ laser, PEG-PCL-IR780+ laser, and PEG-PCL-IR 780-TPZ + laser) received an intravenous injection of ^{18}F-fluoromisonidazole (^{18}F-FMISO, 75 μCi/mouse, 100 μL). Afterward, the tumor hypoxia in mice was photographed using the Inveon small animal PET/CT system

(Siemens, PA). All images were reconstructed with Inveon Software (Siemens, PA).

Lung metastasis evaluation

The lung metastasis inhibition was investigated using the artificial mimic lung metastatic model established as above-described. Specifically, 22 days after therapy, the lung metastatic mice were humanely sacrificed. The lungs were collected and washed. Lung metastases were indicated by the visible white nodules in the excised lungs. The number of lung metastatic nodules was carefully counted through an Olympus microscope. H&E staining of the excised lungs soaked in solution (4% w/v paraformaldehyde) was also employed to assess the histology and pathology.

Evaluation of in vivo antitumor immunity

To assess the in vivo antitumor immunity, the sections of tumor tissue were stained using immunofluorescence for CRT. The infiltration of CD8+ T cells in the tumor was investigated using immunohistochemistry (IHC). Briefly, tumor tissues were harvested and further digested into discrete single cells. Subsequently, the discrete cells were aspirated from suspensions and labeled using PerCP-conjugated anti-mouse CD86 antibody, and FITC-conjugated anti-mouse CD11c antibody to identify the mature DCs. APC-conjugated anti-mouse CD8 antibody, FITC-conjugated anti-mouse CD4 antibody, and PE-conjugated anti-mouse CD69 antibody were used to identify the CD8+ cells and CD4+ T cells, respectively. Finally, the flow cytometry was utilized to identify the activated effector cells.

In vivo biochemical assay

Mouse blood and tissue were collected into a sodium Ethylene Diamine Tetraacetic Acid (EDTA) anticoagulant tube to assess the cytotoxicity of PEG-PCL-IR780-TPZ NPs in vivo. The biochemical analysis was conducted to detect the system side-effect in vivo, including levels of red blood cell (RBC), white blood cell (WBC), hemoglobin concentration (HGB), mean corpuscular hemoglobin content (MCH), and mean corpuscular hemoglobin concentration (MCHC). The level of platelets (PLT) was an important index for evaluating the spleen function.

Statistical analysis

All statistical analyses were carried out using one-way ANOVA. All data were shown as means±standard deviation. *P-value <0.05 represented the significant differences.

Results and discussion

Characterization of the PEG-PCL-IR780-TPZ NPs

The morphology of PEG-PCL NPs and PEG-PCL-IR 780-TPZ NPs is shown in Figure 2A and B. The average size of PEG-PCL NPs was very close to that of PEG-PCL-IR780-TPZ NPs. As exhibited in Figure 2C, the mean hydrodynamic diameter of PEG-PCL-IR780-TPZ NPs was about 135 nm, which was little larger than that of PEG-PCL NPs (125 nm). The absorption spectra showed that PEG-PCL had no remarkable peaks in NIR window (Figure 2D). However, the UV-vis spectra of PEG-PCL-IR780-TPZ NPs had two peaks, which attributed to TPZ and IR780, evidencing the successful encapsulation of TPZ and IR780 in PEG-PCL NPs. Figures S1 and S2 exhibited the absorption curves of IR780 and TPZ with different concentrations, respectively. Based on the earlier data, the standard absorbance versus concentration curves of IR780 and TPZ was quantified (Figures S3 and S4). The drug loading and encapsulation efficiency for IR780 (3.28%, 70.23%) and TPZ (3.33%, 71.28%) in PEG-PCL-IR780-TPZ NPs were calculated. Considering the stability of drug delivery system (DDS) is a precondition for in vivo application, serum or PBS was mixed with PEG-PCL-IR780-TPZ NPs at 37°C to mimic the in vivo physiological condition. As depicted in Figure 2E, no obvious changes in size were noticed during a period of 8 days, illustrating the outstanding stability of PEG-PCL-IR780-TPZ NPs as a DDS. The drug release was an important role for intelligent DDS. It was reported that excessive ROS impair PEG-PCL, thus leading to the subsequent cargo release. IR780 as NIR photosensitizers are capable of generating singlet oxygen (one type of ROS). We speculated whether PEG-PCL-IR780-TPZ NPs could rapidly release IR780 once exposed to the irradiation of an 808 nm laser. As depicted in Figure 2F and Figure S5, no remark release of IR780 and TPZ from PEG-PCL-IR 780-TPZ NPs was detected without the laser irradiation, suggesting that PEG-PCL-IR780-TPZ NPs were considerably stable in circulation. In contrast, with the irradiation of an 808 nm laser, PEG-PCL-IR780-TPZ NPs were rapidly disintegrated, thus robustly and effectively unleashing IR780 and TPZ.

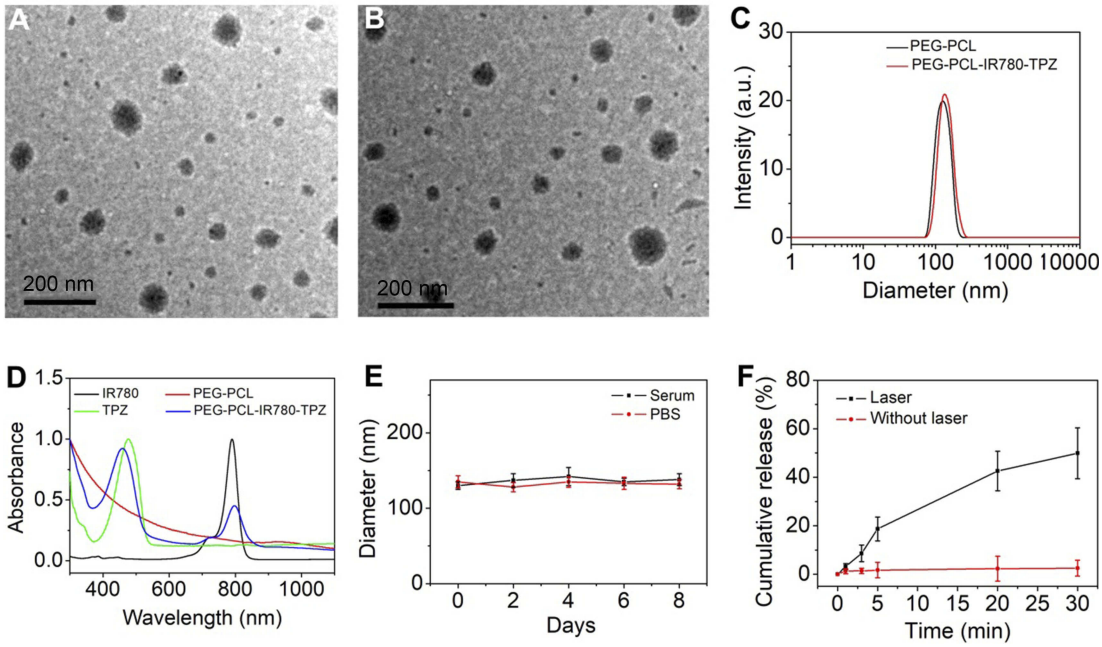

Figure 2 (**A**) Transmission electron microscopy (TEM) photograph of PEG-PCL NPs. (**B**) TEM photograph of PEG-PCL-IR780-TPZ NPs. (**C**) Dynamic light scattering (DLS) of PEG-PCL NPs and PEG-PCL-IR780-TPZ NPs. (**D**) UV-vis-NIR absorption spectra of PEG-PCL (deionized water as solvent), IR780 (dichloromethane as solvent), TPZ (dichloromethane as solvent), and PEG-PCL-IR780-TPZ NPs (deionized water as solvent). (**E**) Stability of PEG-PCL-IR780-TPZ NPs in fetal bovine serum (FBS) or phosphate buffer saline (PBS) was monitored by the DLS technology. (**F**) The release profile of polyethylene glycol- polycaprolactone-2-[2-[2-Chloro-3-[(1,3-dihydro-3,3-dimethyl-1-propyl-2H-indol-2-ylidene)ethylidene]-1-cycloxen-1-yl]-ethenyl]-3,3-dimethy-1-propyl-1H-indolium iodide-tirapazamine nanoparticles (PEG-PCL-IR780-TPZ NPs) under an 808 nm laser irradiation (1 W/cm^2).

In vitro photothermal and photodynamic property of PEG-PCL-IR780-TPZ NPs

In vitro photothermal property of PEG-PCL-IR780-TPZ NPs was assessed using an IR camera. A power-dependent, concentration-dependent, and time-dependent photothermal transformation curves were, respectively, displayed in Figure 3A–C. From these data, PEG-PCL-IR780-TPZ NPs were highlighted to be a potential agent for photothermal therapy. In vitro photodynamic property of PEG-PCL-IR780-TPZ NPs was investigated by assessing ROS level using a ROS/hypoxia ELISA Kit. The kit includes fluorogenic probes for hypoxia (red) and ROS (green). Red hypoxia detection probe is a non-fluorescent or weakly fluorescent aromatic compound containing a nitro (NO_2) moiety. Due to a nitroreductase activity present in hypoxic cells, the nitro group is converted in a series of chemical steps to hydroxylamine (NHOH) and amino (NH_2) group, the original molecule then degrades releasing the fluorescent probe. The ROS reagent is a non-fluorescent, cell-permeable total ROS detection dye which reacts directly with a wide range of reactive species, such as hydrogen peroxide, peroxynitrite, and hydroxyl radicals, yielding a green fluorescent product indicative of cellular production of different ROS/RNS types. As indicated in Figure 3D, no visual fluorescence was observed in the control group, suggesting neither ROS nor hypoxia in 4T1 cells. After co-culture of 4T1 cells with IR780, PEG-PCL-IR780 NPs, and PEG-PCL-IR780-TPZ NPs and irradiated by an 808 nm laser (1 W/cm^2), both green and red fluorescence were revealed, which represented the emergences of ROS and hypoxia. Additionally, we also employed TEMP spin-trapping EPR technology for the singlet oxygen detection. As indicated in Figure S6, characteristic peaks ascribed to singlet oxygen were both observed in IR780 and PEG-PCL-IR780-TPZ NPs, illustrating the generation of ROS and demonstrating the feasibility of PEG-PCL-IR780-TPZ NPs for PDT treatment. Based on the decomposition rate of Na_2-ADPA by PEG-PCL-IR780-TPZ NPs and ICG as well as the absorbance intensity change of Na_2-ADPA at 378 nm (Figures S7 and S8), $^1O_2$ quantum yield of PEG-PCL-IR780-TPZ NPs was calculated to be about 0.235. Moreover, in vitro ROS detection was also conducted in normoxia 4T1 cells (20% oxygen concentration) or hypoxia 4T1 cells (0.05–0.1%

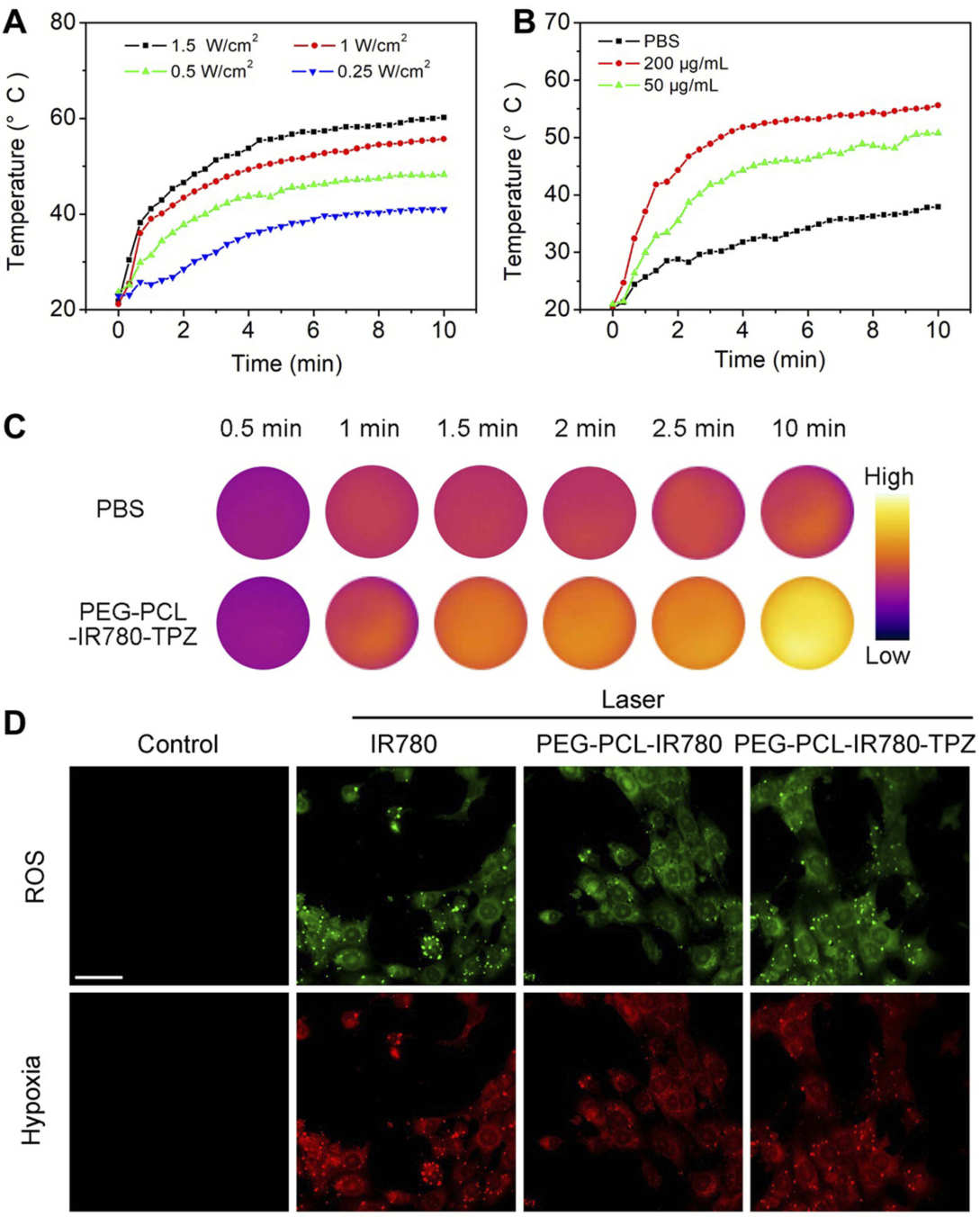

Figure 3 (**A**) The temperature rising profiles of PEG-PCL-IR780-TPZ NPs (the concentration of IR780 was 200 μg/mL) subjected to the irradiation of an 808 nm laser with different power densities for 10 mins. (**B**) The temperature rising profiles of PEG-PCL-IR780-TPZ NPs with different concentrations of IR780 irradiated with an 808 nm laser (1 W/cm^2, 10 mins). (**C**) In vitro temperature elevation photographs of PEG-PCL-IR780-TPZ NPs irradiated with an 808 nm laser (the concentration of IR780, 200 μg/mL, 1 W/cm^2, 10 mins). (**D**) In vitro reactive oxygen species (ROS)/hypoxia detection of 4T1 cells subjected to various treatments. Scale bar: 20 μm.

Abbreviations: PEG-PCL-IR780-TPZ NPs, polyethylene glycol- polycaprolactone-2-[2-[2-Chloro-3-[(1,3-dihydro-3,3-dimethyl-1-propyl-2H-indol-2-ylidene)ethylidene]-1-cycloxen-1-yl]-ethenyl]-3,3-dimethy-1-propyl-1H-indolium iodide-tirapazamine nanoparticles; PBS, phosphate buffer saline.

oxygen concentration) incubated with PEG-PCL-IR 780-TPZ NPs under the irradiation of laser with H_2 DCFDA probe as the ROS indicator. From Figure S9, we could find that ROS only generated in normoxia 4T1 cells, indicating ROS generation in PEG-PCL-IR 780-TPZ NPs was at the cost of oxygen. These results indicated PEG-PCL-IR780-TPZ NPs had wonderful photodynamic property and they consumed the free oxygen (O_2) during the PDT process, causing a hypoxic tumor microenvironment.

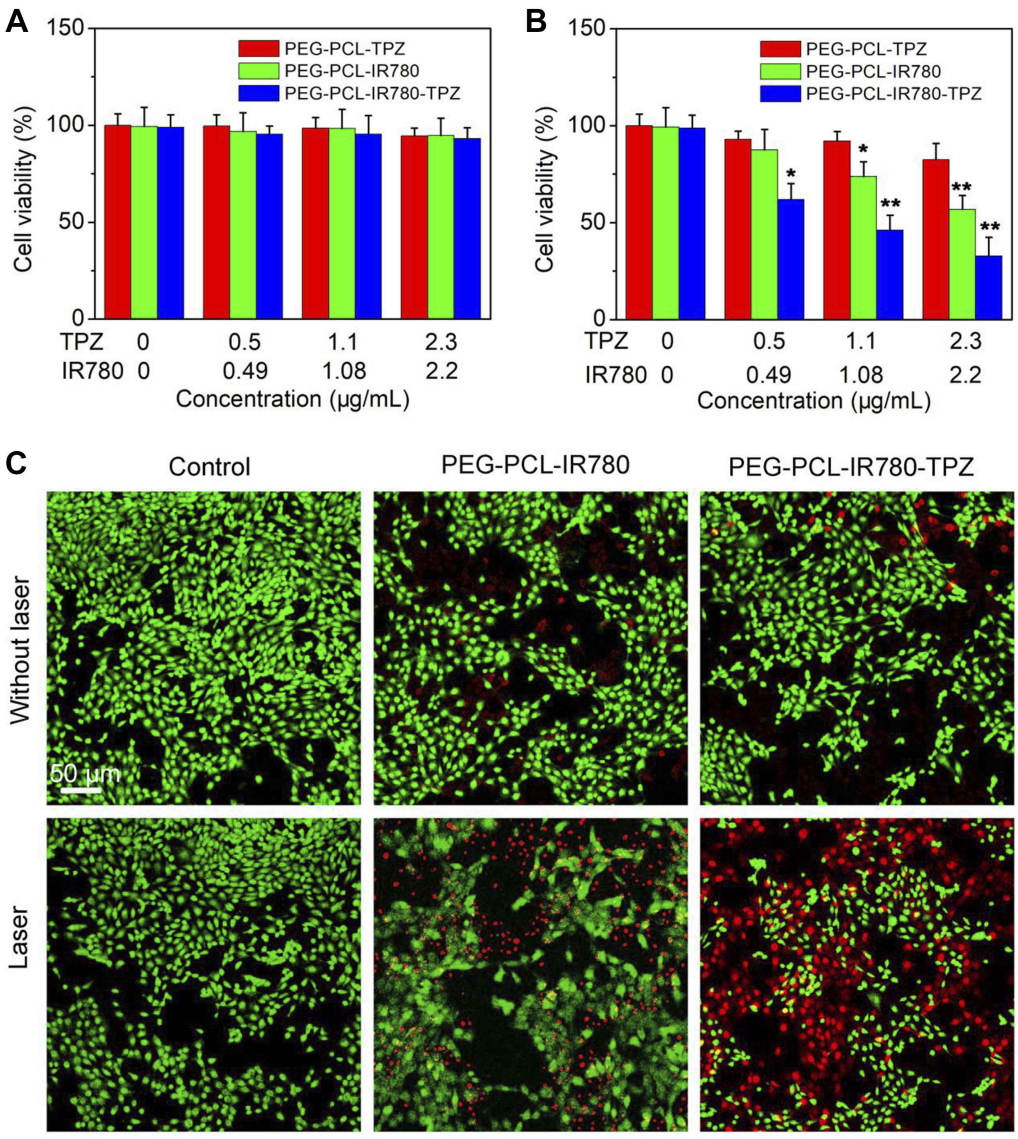

Figure 4 (**A**) The cell viability of 4T1 cells incubated with different particles without a laser irradiation. (**B**) The cell viability of 4T1 cells incubated with different particles with a laser irradiation at the power density of 1 W/cm^2 for 5 mins. *p<0.05, **p<0.01. (**C**) Live/dead examination of 4T1 cells subjected to different treatments was conducted using calcein-acetoxymethyl ester/propidium iodide (Calcein-AM/PI) double staining and observing by confocal laser scanning microscopy (CLSM). Scale bar: 50 μm.

Abbreviations: PEG-PCL-IR780-TPZ NPs, polyethylene glycol-polycaprolactone-2-[2-[2-Chloro-3-[(1,3-dihydro-3,3-dimethyl-1-propyl-2H-indol-2-ylidene)ethylidene]-1-cycloxen-1-yl]-ethenyl]-3,3-dimethy-1-propyl-1H-indolium iodide-tirapazamine nanoparticles.

In vitro antitumor efficacy

Bearing negligible system toxicity is a precondition for in vivo application, thus we assessed the cell viability in IR780, PEG-PCL-IR780 NPs, and PEG-PCL-IR780-TPZ NPs groups without laser irradiation. From Figure 4A, no significant cell toxicity was identified in all groups without the addition of laser irradiation. The cell viability of all groups was above 90%, even at the highest concentration (TPZ, 2.3 μg/mL, IR780, 2.2 μg/mL). On the contrary, the engagement of an 808 nm laser (5 mins, 1 W/cm^2) would be game changing and IR780, PEG-PCL-IR780 NPs, and PEG-PCL-IR780-TPZ NPs groups all compromised cell viability (Figure 4B). In PEG-PCL-IR780 group, when the IR780 concentration increased up to 2.2 μg/mL, the cell viability declined to 56.8%±7.2%. Particularly, the additional engagement of TPZ in PEG-PCL-IR780-TPZ NPs group exhibited better antitumor outcome. When PEG-PCL-IR780-TPZ NPs increased to the highest concentration (TPZ, 2.3 μg/mL, IR780, 2.2 μg/mL), cell viability was 32.7%±9.6%. As a prodrug, TPZ has no system toxicity in normal condition while hypoxic microenvironment could active TPZ and produce the toxic oxidizing

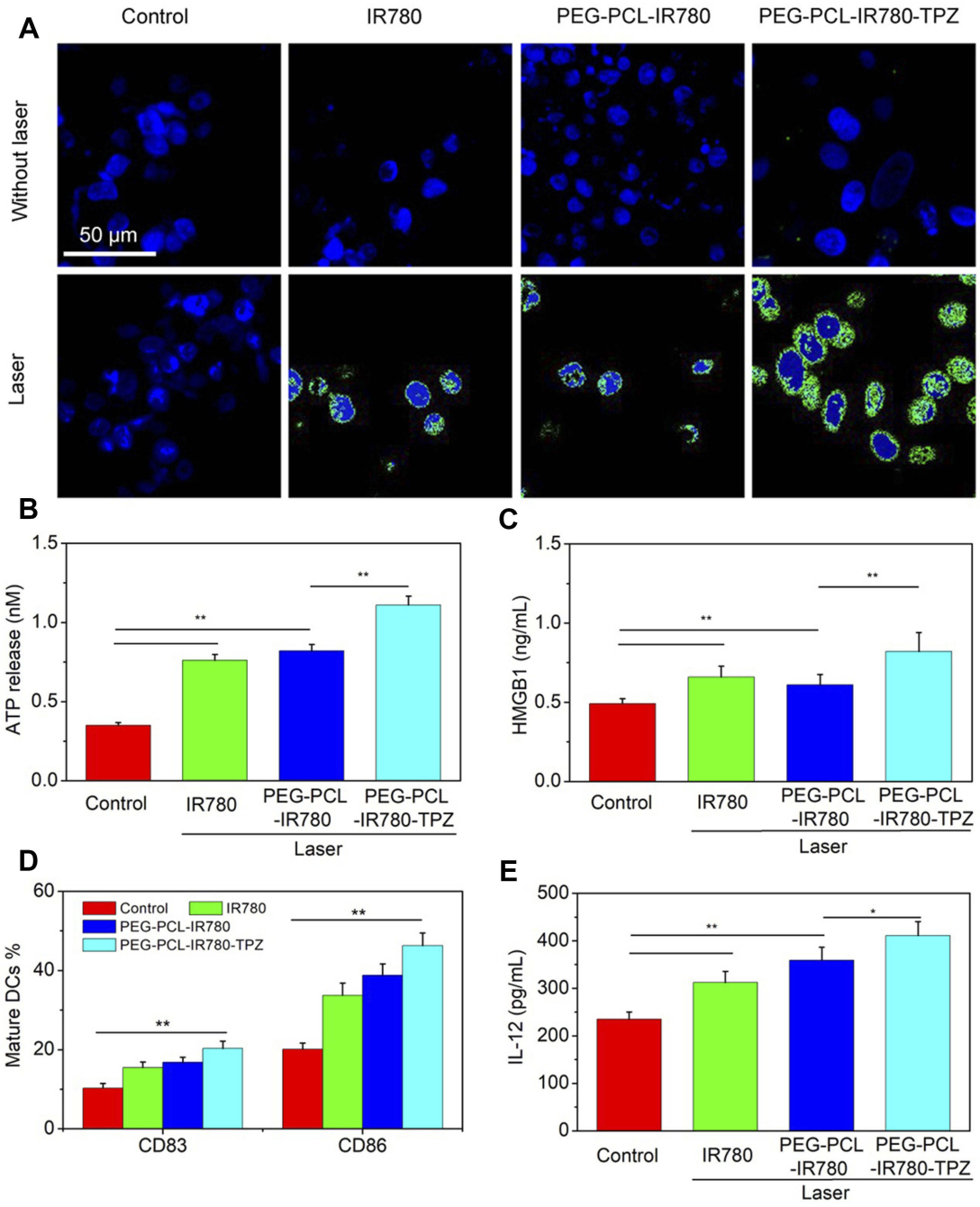

Figure 5 (**A**) The immunogenic cancer cell death (ICD) of 4T1 cells subjected to different treatments was assessed by immunofluorescence staining. Scale bars: 50 μm. (**B**) The release of ATP from dying 4T1 cells subjected to different treatments. (**C**) The release of HMGB1 from dying 4T1 cells subjected to different treatments. (**D**) The evaluation of biomarkers (CD83+CD86+) expression on mature DCs membrane after different treatments. (**E**) The expression level of interleukin 12 (IL-12) from mature DCs after different treatments, *$p<0.05$, **$p<0.01$ (n=3).

Abbreviations: DC, dendritic cells; HMGB1, high-motility group box 1; ATP, adenosine triphosphate; PEG-PCL-IR780-TPZ NPs, polyethylene glycol- polycaprolactone-2-[2-[2-Chloro-3-[(1,3-dihydro-3,3-dimethyl-1-propyl-2H-indol-2-ylidene)ethylidene]-1-cycloxen-1-yl]-ethenyl]-3,3-dimethy-1-propyl-1H-indolium iodide-tirapazamine nanoparticles.

radicals.[54,60] We have demonstrated the capacity of PEG-PCL-IR780-TPZ NPs to cause a serious hypoxic microenvironment. Therefore, the combinational encapsulation of IR780 and TPZ provided favorable potential for hypoxia-activated chemotherapy. Meanwhile, PEG-PCL-IR780-TPZ NPs achieved a synergistic effect of phototherapy and hypoxia-activated chemotherapy. Calcein-AM/PI co-staining was performed to further assess the in vitro

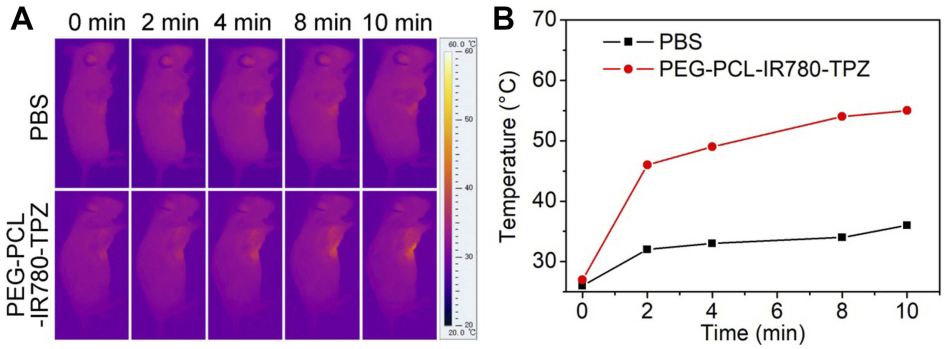

Figure 6 (**A**) In vivo infrared (IR) imaging of 4T1-tumor-bearing mice intravenously injected with PBS or PEG-PCL-IR780-TPZ NPs and irradiated with an 808 nm laser for 10 mins at the power density of 1 W/cm^2. (**B**) Heating curve of 4T1-tumor-bearing mice intravenously injected with PBS or PEG-PCL-IR780-TPZ NPs and irradiated with an 808 nm laser for 10 mins at the power density of 1 W/cm^2.

Abbreviations: PBS, phosphate buffer saline; PEG-PCL-IR780-TPZ NPs, polyethylene glycol-polycaprolactone-2-[2-[2-Chloro-3-[(1,3-dihydro-3,3-dimethyl-1-propyl-2H-indol-2-ylidene)ethylidene]-1-cycloxen-1-yl]-ethenyl]-3,3-dimethy-1-propyl-1H-indolium iodide-tirapazamine nanoparticles.

therapy outcome. The red fluorescence represented dead cells while the green fluorescence indicated live cells. As illustrated in Figure 4C, no obvious red fluorescence was detected in each group without the help of laser irradiation. Nonetheless, each group reflected red fluorescence to different extents when they were irradiated by laser. In particular, PEG-PCL-IR780-TPZ NPs showed the maximum cell death, indicating its excellent synergistic antitumor effect.

In vitro evaluation of induced ICD

Very recently, ICD has drawn exploding attention owing to its robust immune response and outstanding outcome in tumor therapeutic. Hence, ICD in different groups was assessed through the examination of ICD markers (CRT, ATP, and HMGB1). As displayed in Figure 5A, PEG-PCL-IR780-TPZ NPs without the irradiation exhibited weaker effects on inducing CRT expression. However, after the irradiation, PEG-PCL-IR780-TPZ NPs group revealed visually higher CRT expression than that of other groups. Similarly, in comparison with other groups, PEG-PCL-IR780-TPZ NPs triggered higher expression in ATP or HMGB1 release (Figure 5B and C) when exposed to laser. Altogether, we identified that PEG-PCL-IR780-TPZ NPs could invoke ICD during the process of synergic phototherapy and hypoxia-activated chemotherapy.

Since we have already verified the generation of ICD markers (CRT, ATP, and HMGB1) in PEG-PCL-IR780-TPZ NPs + laser group, DCs maturation stimulated by these ICD markers were subsequently evaluated using flow cytometry. As depicted in Figure 5D, expression levels of CD83 and CD86 on cell surface under the treatment of PEG-PCL-IR780-TPZ NPs + laser were remarkably elevated compared with IR780+ laser group and PEG-PCL-IR780 NPs + laser group, implying much pronounced DCs maturation. Furthermore, the expression of IL-12 as a signal cytokine for DCs maturation was tested. As indicated in Figure 5E, PEG-PCL-IR780-TPZ NPs + laser significantly improved the level of IL-12 compared with that of other groups. All these results illustrated that the synergic therapy rendered by PEG-PCL-IR780-TPZ NPs + laser could fully induce ICD and DCs maturation.

In vivo IR imaging of PEG-PCL-IR780-TPZ NPs

Encouraged by in vitro photothermal conversion efficiency, the PTT properties of PEG-PCL-IR780-TPZ NPs on 4T1-tumor-bearing mice were further evaluated. Briefly, 4T1-tumor-bearing mice were intravenously injected with PBS (100 μL) or PEG-PCL-IR780-TPZ NPs (100 μL, 1.5 mg/kg, according to IR780). According to the results in Figure 6A and B, mice in control group exhibited a negligible temperature elevation after exposing to an 808 nm laser irradiation for 10 min. However, the temperature of local tumor position reached to 46°C at 2 mins after injection with PEG-PCL-IR780-TPZ NPs and irradiation with an 808 nm laser. Noteworthy, tumor temperature increased up to 54°C within 10 mins, providing an optimal temperature for tumor ablation and ICD production.[36]

In vivo antitumor effect

Considering the excellent in vitro antitumor properties of PEG-PCL-IR780-TPZ NPs, the therapy efficacy of tumor

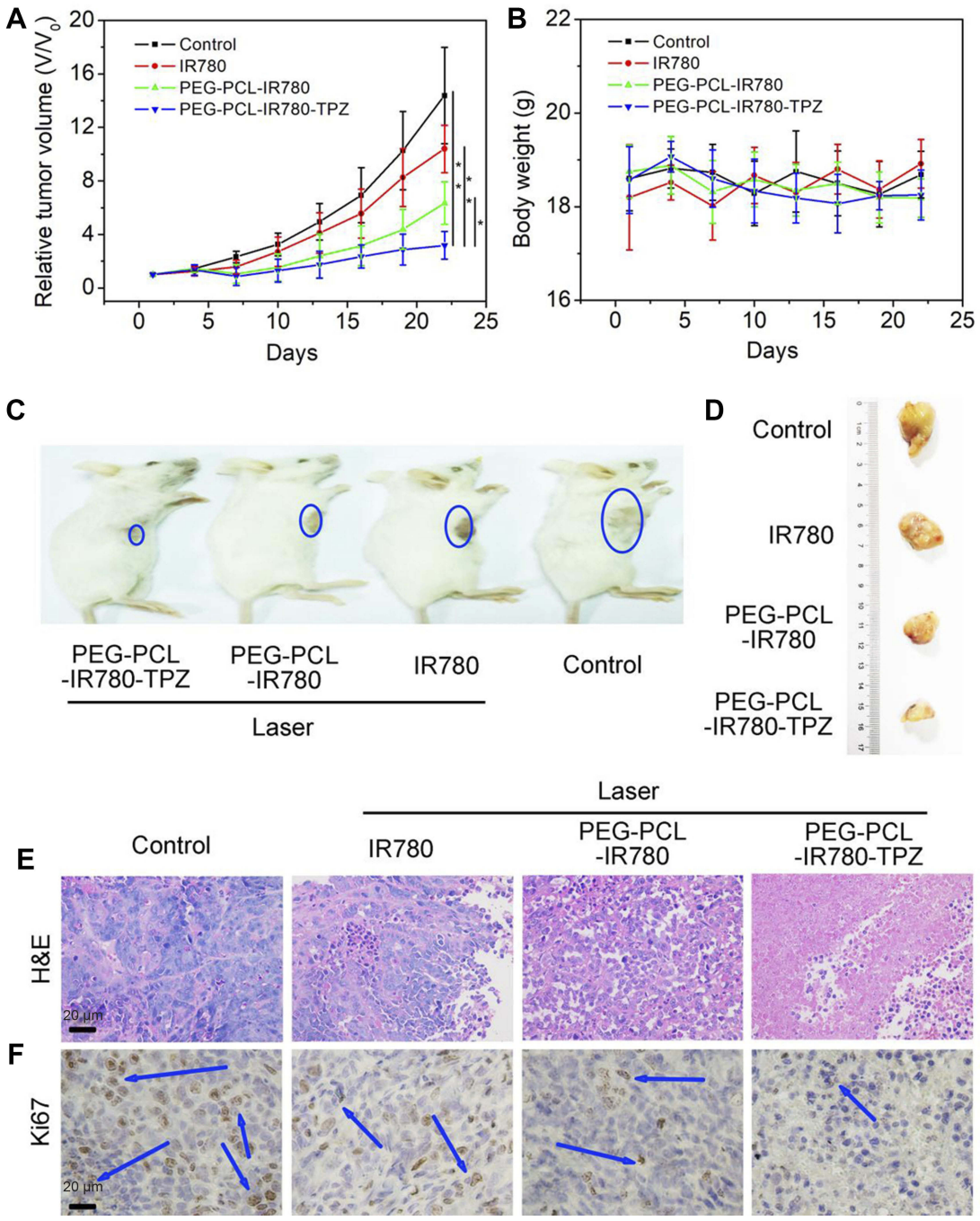

Figure 7 (**A**) Tumor volume growth curves of 4T1-tumor-bearing mice subjected to various treatments (*p<0.05, **p<0.01, n=6). (**B**) Mice weight of 4T1-tumor-bearing mice subjected to various treatments. (**C**) Representative images of 4T1-tumor-bearing mice subjected to various treatments. (**D**) Representative images of tumor tissues separated from 4T1-tumor-bearing mice subjected to various treatments. (**E**) Hematoxylin-eosin (H&E) staining for tumor tissue slices of different groups. (**F**) Ki67 staining for tumor tissue slices of different groups. Blue arrows indicate the positive expression of proliferation marker Ki67.

Abbreviations: PEG-PCL-IR780-TPZ NPs, polyethylene glycol-polycaprolactone-2-[2-[2-Chloro-3-[(1,3-dihydro-3,3-dimethyl-1-propyl-2H-indol-2-ylidene)ethylidene]-1-cycloxen-1-yl]-ethenyl]-3,3-dimethy-1-propyl-1H-indolium iodide-tirapazamine nanoparticles.

was further investigated. Briefly, 4T1-tumor-bearing mice were randomly divided into four groups, including PBS (100 μL), IR780 (100 μL, 1.5 mg/kg, according to IR780), PEG-PCL-IR780 (100 μL, 1.5 mg/kg, according to IR780), PEG-PCL-IR780-TPZ (100 μL, 1.5 mg/kg, according to IR780). As depicted in Figure 7A, PEG-PCL-IR780-TPZ NPs displayed the greatest tumor inhibition among all treated groups. As displayed in Figure 7B, mouse body weight had no apparent changes after different treatments relative to other groups, suggesting no acute toxicity of PEG-PCL-IR

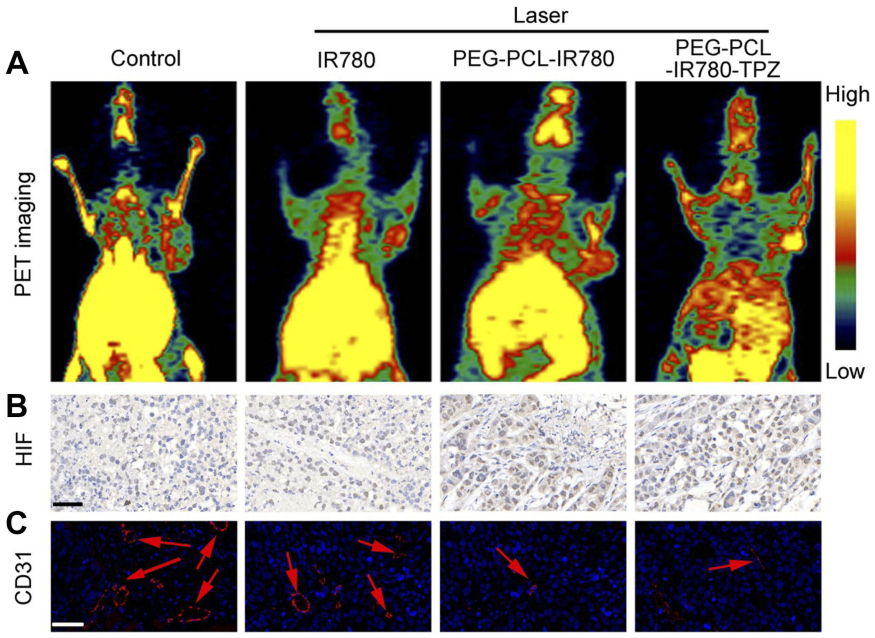

Figure 8 (**A**) Positron Emission Tomography (PET) images of mice recorded after treating with various treatments. (PBS, IR780+ laser, PEG-PCL-IR780+ laser, and PEG-PCL -IR780-TPZ + laser) (**B**) Hypoxia-inducible factor-1α (HIF-1α) staining for tumor tissues of different treatment groups. Scale bars: 50 μm. (**C**) Platelet endothelial cell adhesion molecule-1 (CD31) staining for tumor tissues of different treatment groups. The red arrows represented blood vessel. Scale bars: 50 μm.
Abbreviations: PEG-PCL-IR780-TPZ NPs, polyethylene glycol- polycaprolactone-2-[2-[2-Chloro-3-[(1,3-dihydro-3,3-dimethyl-1-propyl-2H-indol-2-ylidene)ethylidene]-1-cycloxen-1-yl]-ethenyl]-3,3-dimethy-1-propyl-1H-indolium iodide-tirapazamine nanoparticles; PBS, phosphate buffer saline.

780-TPZ NPs. Figure 7C and D showed the representative images of 4T1-tumor-bearing mice and separated primary tumor tissues, respectively. These data suggested the best therapeutic outcome in PEG-PCL-IR780-TPZ NPs group. From the H&E staining images (Figure 7E) and Ki67 staining images (Figure 7F), the largest areas of necrosis and the least proliferation rate in PEG-PCL-IR780-TPZ NPs group were illustrated. Accordingly, we concluded that the synergic phototherapy and hypoxia-activated chemotherapy had a wonderful antitumor efficacy.

In vivo hypoxia detection

In light of above results, PEG-PCL-IR780-TPZ NPs exhibited a superior therapeutic outcome for primary tumor ablation compared with PEG-PCL-IR780 NPs. We deduced that the surprising phenomenon was attributed to the hypoxia-activated chemotherapy rendered by TPZ, which could produce the toxic oxidizing radicals under relative tumor hypoxic microenvironment. To evidence the abovementioned hypothesis, in vivo PET imaging, immunohistochemically staining (hypoxia-inducible factor (HIF)-1α), and immunofluorescence staining (CD31) were carried out to evaluate the tumor hypoxia, respectively. As depicted in Figure 8A, PEG-PCL-IR780 NPs and PEG-PCL-IR780-TPZ NPs caused more significant oxygen depletion than control group and IR780 treatment group. Similarity, compared with control and IR780 group, more serious hypoxia degree reflected by (HIF)-1α staining was detected in PEG-PCL-IR780 NPs and PEG-PCL-IR780-TPZ NPs groups (Figure 8B), which were attributed to the effective tumor enrichment and oxygen consumption of IR780. Moreover, tumor angiogenesis that supplied the adequate oxygen to tumor was further monitored through CD31 staining. Obviously, tumor blood vessels were damaged severely in PEG-PCL-IR780 NPs and PEG-PCL-IR780-TPZ NPs groups compared with control and IR780 group, which were responsible for serious hypoxia level in tumor (Figure 8C). Collectively, all the abovementioned evidences supported that the PEG-PCL-IR780-TPZ NPs could aggravate tumor hypoxia with the help of the irradiation of an 808 nm laser, which subsequently activated the prodrug TPZ and finally featured synergic phototherapy and hypoxia-activated chemotherapy.

Evaluation of PEG-PCL-IR780-TPZ NPs against metastasis in vivo

Fatal metastasis remains a huge challenge for traditional therapy strategies, which is the major reason for cancer deaths. Enlightened by the surprising therapeutic efficacy in vitro and in vivo, we further investigated the effects of nanoparticle-based synergic treatment on triggering the

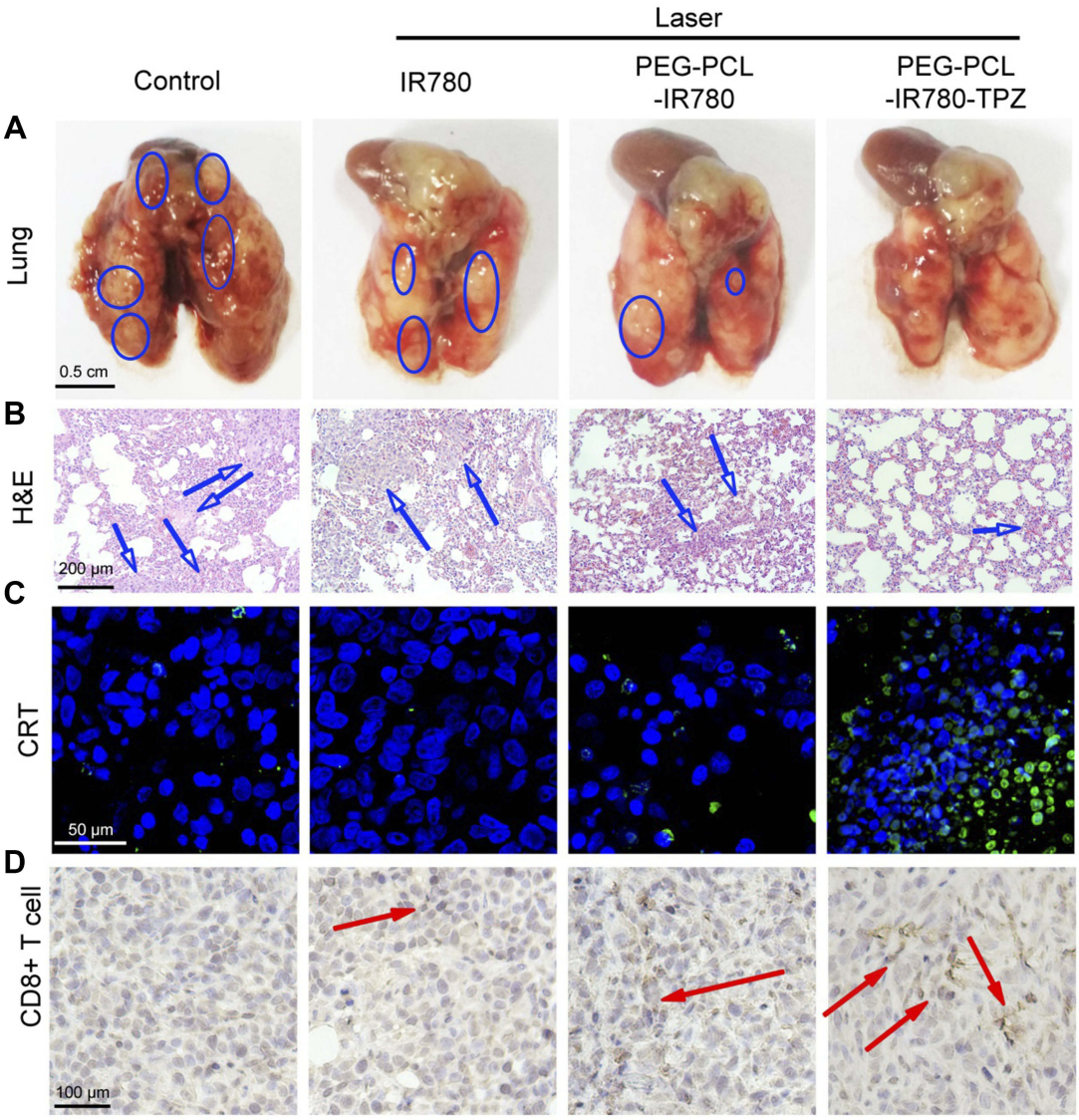

Figure 9 (**A**) Representative lung images showed the metastatic lesions in different treatment groups. The blue circles represented metastatic lesions on lung. Scale bars: 0.5 cm. (**B**) H&E staining for lung tissues of different treatment groups. Blue arrows indicate apoptosis and necrosis. Scale bars: 200 μm. (**C**) Ex vivo immunofluorescence indicated the level of CRT expression in primary tumor tissues. The green area indicated CRT while the blue area indicated cell nuclei. Scale bars: 50 μm. (**D**) The activated CD8+ T-cell infiltrated into tumor tissues after treating with different treatments. The red arrow represented the CD8+ T-cells. Scale bars: 100 μm.

Abbreviations: PEG-PCL-IR780-TPZ NPs, polyethylene glycol- polycaprolactone-2-[2-[2-Chloro-3-[(1,3-dihydro-3,3-dimethyl-1-propyl-2H-indol-2-ylidene)ethylidene]-1-cycloxen-1-yl]-ethenyl]-3,3-dimethy-1-propyl-1H-indolium iodide-tirapazamine nanoparticles; CRT, calreticulin.

abscopal effect against metastasis. As shown in Figure 9A, the size and number of tumor nodules in mouse lungs of control group were the greatest than that of other groups and PEG-PCL-IR780-TPZ NPs + laser treatment led to a dramatical decrease in the number of metastatic nodules compared to IR780+ laser and PEG-PCL-IR780 NPs + laser treatments. PEG-PCL-IR780-TPZ NPs + laser treatment had the maximum ability to alleviate tumor metastasis than other treatments (Figure 9B). Collectively, we demonstrated that synergic phototherapy and hypoxia-activated chemotherapy rendered by PEG-PCL-IR780-TPZ NPs + laser could ablate the primary tumor and control the tumor metastasis.

ICD-mediated antitumor immunity in vivo

We hypothesized that the visual inhibition of tumor metastasis in PEG-PCL-IR780-TPZ NPs + laser group could be explained by the fact that synergic phototherapy and hypoxia-activated chemotherapy would induce antitumor immune responses through the generation of ICD. As indicated in Figure 9C, CRT level on tumor cell surfaces induced by PEG-PCL-IR780-TPZ NPs under an 808 nm laser irradiation was higher than that of IR780 and PEG-PCL-IR780 NPs, which mainly attributed to synergic phototherapy and hypoxia-activated chemotherapy favoring antitumor immune responses. After that, the

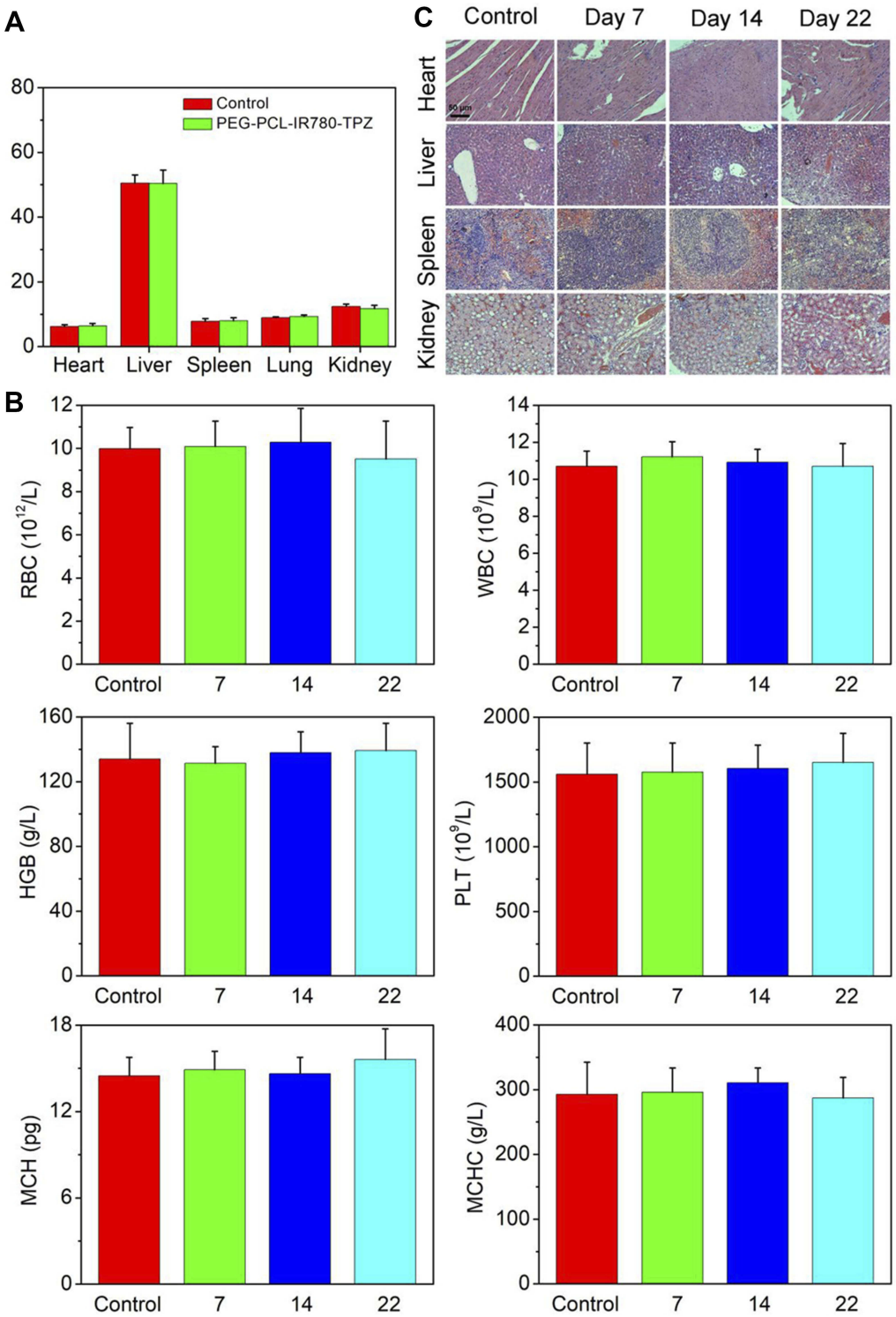

Figure 10 Long-term safety study. (**A**) Weight ratio of major tissues (heart, liver, spleen, lung, kidney) to mice body. (**B**) The relevant blood analysis. (**C**) H&E staining as a pathologic analysis for major organs (n=3). Scale bar: 50 μm.

Abbreviations: PEG-PCL-IR780-TPZ NPs, polyethylene glycol- polycaprolactone-2-[2-[2-Chloro-3-[(1,3-dihydro-3,3-dimethyl-1-propyl-2H-indol-2-ylidene)ethylidene]-1-cycloxen-1-yl]-ethenyl]-3,3-dimethy-1-propyl-1H-indolium iodide-tirapazamine nanoparticles; RBC, red blood cell; WBC, white blood cell; HGB, hemoglobin concentration; MCH, mean corpuscular hemoglobin content; MCHC, mean corpuscular hemoglobin concentration; PLT, platelets.

biomarkers (CD11c+CD86+) as the signal for mature DCs were evaluated using FCM and exhibited in Figure S10. The data showed higher levels of biomarkers on DC cell surface in the PEG-PCL-IR780-TPZ NPs group. Meanwhile, the activated-T lymphocytes infiltrated into tumor tissues was investigated and depicted in Figure 9D

and Figure S11. According to immunohistochemistry (Figure 9D), brown signals indicated infiltration of activated CD8+ T cells into tumors, and it was the most pronounced in PEG-PCL-IR780-TPZ NPs group. The effector cells including CD8+ and CD4+ T cells were further assessed by staining with antibodies and conducted using FCM (Figure S6). Similarly, more effector cells were witnessed in PEG-PCL-IR780-TPZ NPs group. Taken together, all the results implied that PEG-PCL-IR 780-TPZ NPs armed by an 808 nm laser irradiation could induce the robust anti-tumor immunity for suppressing tumor metastases.

Safety evaluation in vivo

The primary safety evaluation was performed after mice were humanely sacrificed. As described in Figure 10A, the weight ratio of major organs to body weight in PEG-PCL-IR 780-TPZ NPs group was similar to that of control group. Moreover, indexes of aerobic capacity and hematopoietic (HGB, RBC, WBC, etc.) had no obvious changes as displayed in Figure 10B. As indicated in Figure 10C, no visible damage was observed in the major tissues. Taken together, ignorable changes or damages were observed in synergic phototherapy and hypoxia-activated chemotherapy rendered by PEG-PCL-IR780-TPZ NPs, suggesting the potential value of PEG-PCL-IR780-TPZ NPs on clinical application.

Conclusion

In summary, we tailor-made PEG-PCL-IR780-TPZ NPs as a versatile nano-platform for cancer treatment. The platform achieved a smart drug delivery, controlled cargo release, and a robust ICD outcome. Especially, the combination of phototherapy and hypoxia-activated chemotherapy could produce damage-associated molecular patterns (DAMPs) including ATP, HMGB1, and CRT as activated endogenous potentiators, subsequently induce DCs maturation and activation of toxic T lymphocytes. As expected, our platform successfully eliminates the primary tumor and controls the development of tumor metastasis, lighting up the clinical application of cancer treatment.

Acknowledgments

This study was supported by the joint funds of the Natural Science Foundation of Xinjiang Uygur Autonomous Region (No. 2016D01C380), and the National Natural science Foundation of China (No. 21764015, No. 11847610, No. 11464047).

Author contributions

All authors contributed to data analysis, drafting and revising the article, gave final approval of the version to be published, and agree to be accountable for all aspects of the work.

Disclosure

The authors report no conflicts of interest in this work.

References

1. Ragaz J, Jackson SM, Le N, et al. Adjuvant radiotherapy and chemotherapy in node-positive premenopausal women with breast cancer. *N Engl J Med*. 1997;337:956–962. doi:10.1056/NEJM199710023371402
2. Chen W, Ouyang J, Liu H, et al. Black phosphorus nanosheet-based drug delivery system for synergistic photodynamic/photothermal/chemotherapy of cancer. *Adv Mater*. 2017;29:1603864. doi:10.1002/adma.201700681
3. Ouyang J, Wang L, Chen W, et al. Biomimetic nanothylakoids for efficient imaging-guided photodynamic therapy for cancer. *Chem Commun*. 2018;54:3468–3471. doi:10.1039/C8CC00674A
4. Bianchini G, Balko JM, Mayer IA, Sanders ME, Gianni L. Triple-negative breast cancer: challenges and opportunities of a heterogeneous disease. *Nat Rev Clin Oncol*. 2016;13:674–690. doi:10.1038/nrclinonc.2016.66
5. Zeng K, Xu Q, Ouyang J, et al. Coordination nanosheets of phthalocyanine as multifunctional platform for imaging-guided synergistic therapy of cancer. *ACS Appl Mater Interfaces*. 2019;11:6840–6849. doi:10.1021/acsami.8b22008
6. Ren S, Yang J, Ma L, et al. Ternary-responsive drug delivery with activatable dual mode contrast-enhanced in vivo imaging. *ACS Appl Mater Interfaces*. 2018;10:31947–31958. doi:10.1021/acsami.8b10564
7. De Palma M, Biziato D, Petrova TV. Microenvironmental regulation of tumour angiogenesis. *Nat Rev Cancer*. 2017;17:457–474. doi:10.1038/nrc.2017.51
8. Ouyang J, Deng Y, Chen W, et al. Marriage of artificial catalase and black phosphorus nanosheets for reinforced photodynamic antitumor therapy. *J Mater Chem B*. 2018;6:2057–2064. doi:10.1039/C8TB00371H
9. Demaria S, Kawashima N, Yang AM, et al. Immune-mediated inhibition of metastases after treatment with local radiation and CTLA-4 blockade in a mouse model of breast cancer. *Clin Cancer Res*. 2005;11:728–734.
10. Sandip Pravin P, Razelle K. PD-L1 expression as a predictive biomarker in cancer immunotherapy. *Mol Cancer Ther*. 2015;14:847–856. doi:10.1158/1535-7163.MCT-14-0983
11. Wang X, Li X, Ito A, Sogo Y, Ohno T. Particle-size-dependent toxicity and immunogenic activity of mesoporous silica-based adjuvants for tumor immunotherapy. *Acta Biomater*. 2013;9:7480–7489. doi:10.1016/j.actbio.2013.03.031
12. Jen-Chieh T, Brandi L, Alicia H, et al. Systemic tumor targeting and killing by sindbis viral vectors. *Nat Biotechnol*. 2004;22:70–77. doi:10.1038/nbt917
13. Carpenter RA, Kwak JG, Peyton SR, Lee J. Implantable pre-metastatic niches for the study of the microenvironmental regulation of disseminated human tumour cells. *Nat Biomed Eng*. 2018;2:915–929. doi:10.1038/s41551-018-0307-x
14. Yu C, Xu L, Chao L, et al. Combined local immunostimulatory radioisotope therapy and systemic immune checkpoint blockade imparts potent antitumour responses. *Nat Biomed Eng*. 2018;2:611–621. doi:10.1038/s41551-018-0262-6
15. Li Y, He L, Dong H, et al. Fever-inspired immunotherapy based on photothermal cpg nanotherapeutics: the critical role of mild heat in regulating tumor microenvironment. *Adv Sci*. 2018;5:1700805–-1700816. doi:10.1002/advs.201700805

16. Chiang CS, Lin YJ, Lee R, et al. Combination of fucoidan-based magnetic nanoparticles and immunomodulators enhances tumour-localized immunotherapy. *Nat Nanotechnol*. 2018;13:746–754. doi:10.1038/s41565-018-0146-7
17. Kim DH, Han JS, Ly P, et al. TRIP13 and APC15 drive mitotic exit by turnover of interphase-and unattached kinetochore-produced MCC. *Nat Commun*. 2018;9:4354–4364.
18. Adachi K, Kano Y, Nagai T, Okuyama N, Sakoda Y, Tamada K. IL-7 and CCL19 expression in CAR-T cells improves immune cell infiltration and CAR-T cell survival in the tumor. *Nat Biotechnol*. 2018;36:346–351. doi:10.1038/nbt.4086
19. Smith TT, Stephan SB, Moffett HF, et al. In situ programming of leukaemia-specific T cells using synthetic DNA nanocarriers. *Nat Nanotechnol*. 2017;12:813–820. doi:10.1038/nnano.2017.57
20. Rodell CB, Arlauckas SP, Cuccarese MF, et al. TLR7/8-agonist-loaded nanoparticles promote the polarization of tumour-associated macrophages to enhance cancer immunotherapy. *Nat Biomed Eng*. 2018;2:578–588.
21. Chen Q, Xu L, Liang C, Wang C, Peng R, Liu Z. Photothermal therapy with immune-adjuvant nanoparticles together with checkpoint blockade for effective cancer immunotherapy. *Nat Commun*. 2016;7:13193. doi:10.1038/ncomms13193
22. Heidi L. Immunotherapy's cancer Remit Widens. *Nature*. 2013;497:544.
23. Liang R, Liu L, He H, et al. Oxygen-boosted immunogenic photodynamic therapy with gold nanocages@manganese dioxide to inhibit tumor growth and metastases. *Biomaterials*. 2018;177:149–160. doi:10.1016/j.biomaterials.2018.05.051
24. Wong ML, Griffiths LG. Immunogenicity in xenogeneic scaffold generation: antigen removal vs. decellularization. *Acta Biomater*. 2014;10:1806–1816. doi:10.1016/j.actbio.2014.01.028
25. Duan X, Chan C, Lin W. Nanoparticle-mediated immunogenic cell death enables and potentiates cancer immunotherapy. *Angew Chem Int Ed*. 2018;58:670–680. doi:10.1002/anie.201804882
26. Kepp O, Galluzzi L, Martins I, et al. Molecular determinants of immunogenic cell death elicited by anticancer chemotherapy. *Cancer Metastasis Rev*. 2011;30:61–69. doi:10.1007/s10555-011-9273-4
27. Lu J, Liu X, Liao YP, et al. Nano-enabled pancreas cancer immunotherapy using immunogenic cell death and reversing immunosuppression. *Nat Commun*. 2017;8:1811. doi:10.1038/s41467-017-01651-9
28. Yang C, Chen Y, Wei G, et al. Bismuth ferrite-based nanoplatform design: an ablation mechanism study of solid tumor and NIR-triggered photothermal/photodynamic combination cancer therapy. *Adv Funct Mater*. 2018;28:1706827. doi:10.1002/adfm.201706827
29. Su YL, Hu SH. Functional nanoparticles for tumor penetration of therapeutics. *Pharmaceutics*. 2018;10:193. doi:10.3390/pharmaceutics10040193
30. Wang C, Xu L, Liang C, Xiang J, Peng R, Liu Z. Immunological responses triggered by photothermal therapy with carbon nanotubes in combination with anti-CTLA-4 therapy to inhibit cancer metastasis. *Adv Mater*. 2014;26:8154–8162. doi:10.1002/adma.201402996
31. Dong K, Liu Z, Liu J, et al. Biocompatible and high-performance amino acids-capped $MnWO_4$ nanocasting as a novel non-lanthanide contrast agent for X-ray computed tomography and T(1)-weighted magnetic resonance imaging. *Nanoscale*. 2014;6:2211–2217. doi:10.1039/c3nr05455a
32. Li T, Yan L. Functional polymer nanocarriers for photodynamic therapy. *Pharmaceuticals*. 2018;11:133. doi:10.3390/ph11040133
33. Liu Z, Liu J, Wang R, Du Y, Ren J, Qu X. An efficient nano-based theranostic system for multi-modal imaging-guided photothermal sterilization in gastrointestinal tract. *Biomaterials*. 2015;56:206–218. doi:10.1016/j.biomaterials.2015.04.005
34. Yang Z, Liu T, Xie Y, et al. Chitosan layered gold nanorods as synergistic therapeutics for photothermal ablation and gene silencing in triple-negative breast cancer. *Acta Biomater*. 2015;25:194–204. doi:10.1016/j.actbio.2015.07.026
35. Chen Y, Li H, Deng Y, Sun H, Ke X, Ci T. Near-infrared light triggered drug delivery system for higher efficacy of combined chemo-photothermal treatment. *Acta Biomater*. 2017;51:374–392. doi:10.1016/j.actbio.2016.12.004
36. Sweeney EE, Cano-Mejia J, Fernandes R. Photothermal therapy generates a thermal window of immunogenic cell death in neuroblastoma. *Small*. 2018;14:e1800678. doi:10.1002/smll.v14.20
37. Lu J, Liu X, Liao YP, et al. Breast cancer chemo-immunotherapy through liposomal delivery of an immunogenic cell death stimulus plus interference in the IDO-1 pathway. *ACS Nano*. 2018;12:11041–11061. doi:10.1021/acsnano.8b05189
38. Adkins I, Fucikova J, Garg AD, Agostinis P, Špíšek R. Physical modalities inducing immunogenic tumor cell death for cancer immunotherapy. *Oncoimmunology*. 2014;3:e968434. doi:10.4161/21624011.2014.968434
39. Zhang L, Wang D, Yang K, et al. Mitochondria-targeted artificial "nano-RBCs" for amplified synergistic cancer phototherapy by a single NIR irradiation. *Adv Sci*. 2018;5:1800049–1800063. doi:10.1002/advs.201800049
40. Spring BQ, Sears RB, Zheng LZ, et al. A photoactivable multi-inhibitor nanoliposome for tumour control and simultaneous inhibition of treatment escape pathways. *Nat Nanotechnol*. 2016;11:378–387. doi:10.1038/nnano.2015.311
41. Liu LH, Zhang YH, Qiu WX, et al. Dual-stage light amplified photodynamic therapy against hypoxic tumor based on an O_2 self-sufficient nanoplatform. *Small*. 2017;13:1701621. doi:10.1002/smll.201701621
42. Peng C-L, Shih Y-H, Lee P-C, Hsieh H, Luo T-Y, Shieh M-J. Multimodal image-guided photothermal therapy mediated by ^{188}re-labeled micelles containing a cyanine-type photosensitizer. *ACS Nano*. 2011;5:5594–5607. doi:10.1021/nn201100m
43. Alves CG, Lima-Sousa R, Melo-Diogo DD, Louro RO, Correia IJ. IR780 based nanomaterials for cancer imaging and photothermal, photodynamic and combinatorial therapies. *Int J Pharm*. 2018;542:164–175. doi:10.1016/j.ijpharm.2018.03.020
44. Yang Y, Yang X, Li H, et al. Near-infrared light triggered liposomes combining photodynamic and chemotherapy for synergistic breast tumor therapy. *Colloids Surf B*. 2019;173:564–570. doi:10.1016/j.colsurfb.2018.10.019
45. Brown JM, Wilson WR. Exploiting tumour hypoxia in cancer treatment. *Nat Rev Cancer*. 2004;4:437–447. doi:10.1038/nrc1367
46. Liu Y, Liu Y, Bu W, et al. Hypoxia induced by upconversion-based photodynamic therapy: towards highly effective synergistic bioreductive therapy in tumors. *Angew Chem Int Ed*. 2015;54:8105–8109. doi:10.1002/anie.201500478
47. Anderson RF, Shinde SS, Hay MP, Gamage SA, Denny WA. Activation of 3-amino-1, 2, 4-benzotriazine 1, 4-dioxide antitumor agents to oxidizing species following their one-electron reduction. *J Am Chem Soc*. 2003;125:748–756. doi:10.1021/ja0209363
48. Kroemer G, Galluzzi L, Kepp O, Zitvogel L. Immunogenic cell death in cancer therapy. *Annu Rev Immunol*. 2013;31:51–72. doi:10.1146/annurev-immunol-032712-100008
49. Galluzzi L, Buqué A, Kepp O, Zitvogel L, Kroemer G. Immunogenic cell death in cancer and infectious disease. *Nat Rev Immunol*. 2016;17:97–111. doi:10.1038/nri.2016.107
50. Kepp O, Senovilla L, Vitale I, et al. Consensus guidelines for the detection of immunogenic cell death. *Oncoimmunology*. 2014;3:e955691. doi:10.4161/21624011.2014.955691
51. Garg AD, Agostinis P. Editorial: immunogenic cell death in cancer: from Benchside research to bedside reality. *Front Immunol*. 2016;7:110. doi:10.3389/fimmu.2016.00110

52. Apetoh L, Ghiringhelli F, Tesniere A, et al. Toll-like receptor 4-dependent contribution of the immune system to anticancer chemotherapy and radiotherapy. *Nat Med*. 2007;13:1050–1059. doi:10.1038/nm1622
53. Casares N, Pequignot MO, Antoine T, et al. Caspase-dependent immunogenicity of doxorubicin-induced tumor cell death. *J Exp Med*. 2005;202:1691–1701. doi:10.1084/jem.20050915
54. Zhao P, Ren S, Liu Y, Huang W, Zhang C, He J. PL-$W_{18}O_{49}$-TPZ nanoparticles for simultaneous hypoxia-activated chemotherapy and photothermal therapy. *ACS Appl Mater Interfaces*. 2018;10:3405–3413. doi:10.1021/acsami.7b17323
55. Le KT, Yu JH, Jun H, et al. Polyglycerolated nanocarriers with increased ligand multivalency for enhanced *in vivo* therapeutic efficacy of paclitaxel. *Biomaterials*. 2017;43:223–232.
56. Jiang C, Cheng H, Yuan A, Tang X, Wu J, Hu Y. Hydrophobic IR780 encapsulated in biodegradable human serum albumin nanoparticles for photothermal and photodynamic therapy. *Acta Biomater*. 2015;14:61–69. doi:10.1016/j.actbio.2014.11.041
57. Wang S, Shang L, Li L, et al. Metal-organic-framework-derived mesoporous carbon nanospheres containing porphyrin-like metal centers for conformal phototherapy. *Adv Mater*. 2016;28:8379–8387. doi:10.1002/adma.201602197
58. Ren H, Liu J, Su F, et al. Relighting photosensitizers by synergistic integration of albumin and perfluorocarbon for enhanced photodynamic therapy. *ACS Appl Mater Interfaces*. 2017;9:3463−3473. doi:10.1021/acsami.6b14885
59. Luo Z, Wang C, Yi H, et al. Nanovaccine loaded with poly I:C and STAT3 siRNA robustly elicits anti-tumor immune responses through modulating tumor-associated dendritic cells in vivo. *Biomaterials*. 2015;38:50–60. doi:10.1016/j.biomaterials.2014.10.050
60. Qian C, Feng P, Yu J, et al. Anaerobe-inspired anticancer nanovesicles. *Angew Chem Int Ed*. 2017;56:2588–2593. doi:10.1002/anie.201611783